Environmental Science Nano

ROYAL SOCIETY OF CHEMISTRY

PAPER

View Article Online
View Journal | View Issue

Cite this: *Environ. Sci.: Nano*, 2025, **12**, 1515

Insights in photocatalytic/Fenton-based degradation of microplastics using iron-modified titanium dioxide aerogel powders†

Guru Karthikeyan Thirunavukkarasu, *[a] Monika Motlochová, [a] Dmytro Bavol,[a] Anna Vykydalová,[a] Jaroslav Kupčík,[a] Michal Navrátil, [a] Kaplan Kirakci, [a] Eva Pližingrová,[a] Dana Dvoranová[b] and Jan Šubrt[a]

Microplastic (MP) pollution has become a serious environmental problem in the current decade. Unfortunately, wastewater treatment plants are not favorable for treating MPs. Therefore, it is necessary to develop methodologies to treat MPs in water efficiently. Photocatalytic (PC) and photo-Fenton (PF) processes are among the promising treatment methodologies that utilize reactive oxygen species (ROS) to degrade MPs. In this study, TiO_2 aerogel powders (TiAP) were prepared by lyophilization and subsequent annealing of peroxo-titanic acid gels, followed by modification with Fe at the surface for the PC/PF-based degradation of MPs. Fe-modification on TiAP boosts the PC activity and activates the PF-based process in the presence of H_2O_2. The degradation of polystyrene (PS) MPs was evaluated using attenuated total reflection infrared (ATR-IR) spectroscopy, total organic carbon (TOC) analysis, thermogravimetric analysis coupled with differential scanning calorimetry and mass spectrometry (TGA-DSC/MS), nuclear magnetic resonance (NMR) spectroscopy, and high-performance liquid chromatography with high-resolution mass spectrometry (HPLC-HRMS). Photo-induced degradation of the PS MPs was evaluated by monitoring the changes in the carbonyl/peroxyl index (CI/PI) recorded by ATR-IR spectroscopy and the mass loss measured by TGA-DSC/MS techniques. Interestingly, the samples with higher CI value changes affected the total mass residue, while samples with lower changes in the CI value did not alter the total mass residue after the photo-induced treatment. Further, NMR spectra confirmed the formation of new peaks due to the oxidative degradation of PS MPs, especially between 0.8 and 1.3 ppm. Additionally, by-products formed after the photo-induced treatment process analyzed by the HPLC-HRMS technique indicate the degradation of PS MPs. The indirect techniques of electron paramagnetic resonance (EPR) spectroscopy revealed the ROS contributing to the oxidation of PS MPs during the PC and PF treatment process using Fe-modified TiAP. This study's findings have the potential to significantly influence future research and environmental policies by providing better insights into preparing efficient nanostructures for photo-induced degradation of MPs.

Received 4th September 2024,
Accepted 14th December 2024

DOI: 10.1039/d4en00818a

rsc.li/es-nano

Environmental significance

Water bodies throughout the world are being affected by microplastics that cause adverse effects on the environment. Conventional water treatment methodologies do not efficiently remove microplastics from water. Therefore, eventually, these microplastics end up in the food cycle and potentially cause harm to all living organisms. This study deals with understanding the use of iron-modified titanium dioxide aerogel powders for the photocatalytic and photo-Fenton-based processes for the efficient degradation of microplastics in water.

1. Introduction

Over the past decades, excessive use and disposal of plastic products have seriously threatened the environment.[1–3] By 2025, around 250 million tons of plastics could be accumulated in rivers and oceans.[3–5] Eventually, these plastics are fragmented into micro/nano sizes through various chemical, physical, and biological processes.[6–9]

[a] *Institute of Inorganic Chemistry of the Czech Academy of Sciences, Husinec-Řež 250 68, Czech Republic. E-mail: thirunavukkarasu@iic.cas.cz*
[b] *Institute of Physical Chemistry and Chemical Physics, Faculty of Chemical and Food Technology, Slovak University of Technology in Bratislava, Bratislava, SK-812 37, Slovak Republic*

† Electronic supplementary information (ESI) available. See DOI: https://doi.org/10.1039/d4en00818a

Plastics with a size range between 5 mm and 1 μm have been classified as microplastics (MPs), whereas less than 1 μm are nanoplastics (NPs).[6,9–11] The toxic additives (plasticizers, pigments, stabilizers, *etc.*) added during plastic manufacturing are ultimately released into the environment during the MP/NP transport cycle.[12] Further, MPs/NPs could also adsorb other toxic organic and inorganic pollutants in the environment, thereby increasing their potency.[7,13,14] Regardless of their size, they are classified as pollutants of emerging concern owing to their toxicity and negative impact on water bodies.[15–17]

Unfortunately, wastewater treatment methodologies in municipal treatment plants are not well equipped to treat water containing MPs/NPs.[18] In fact, these municipal treatment plants are one of the sources of microplastic pollutants.[19,20] Currently, techniques such as physical separation (membrane separation, adsorption, and coagulation), biological techniques (membrane bioreactors and biological degradation), and advanced oxidation processes (photocatalytic (PC) process, Fenton-based process, and ozonation) are being developed for the treatment of MPs/NPs in water.[21–24] Physical separation techniques are non-destructive in nature, *i.e.*, MPs/NPs are transferred from the water to another medium (filters, adsorbents/coagulants), whereas biological treatment methodologies require optimal environmental conditions.[10] However, eliminating MPs/NPs by degrading them to non-toxic products through an advanced oxidative degradation process is a more efficient process than the physical separation of MPs.[10,11,21,22] Moreover, reaction conditions such as treatment time, catalyst concentration, and light intensity could be manipulated based on the pollutant type and treatment methodologies.[25]

Generally, oxidative degradation of MPs by photoaging *via* the generation of reactive oxygen species (ROS) is very slow, and hence, the UV/H_2O_2 system was introduced to enhance their degradation.[26,27] But still, even with the addition of H_2O_2, the degradation of microplastics could take days.[27] Hence, photocatalysts were used to enhance the degradation of microplastics.[28] The TiO_2 semiconductor is a popular photocatalyst worldwide due to its non-toxicity, availability, recyclability, and affordability.[29] TiO_2 exists in three polymorphs (anatase, rutile, and brookite), where anatase is the most suitable for photocatalytic degradation of organic pollutants.[29–31] Upon irradiation of light of suitable wavelength (λ = 275 to 405 nm) on TiO_2, e^-/h^+ are produced, which subsequently react with surface water and oxygen to form ROS.[32–35] The hydroxyl radical ($HO^\bullet$) is the main ROS species responsible for the decomposition of pollutants.[32–36] This process of pollutant degradation has been used for the degradation of various complex organic pollutants.[35] L. P. Domínguez-Jaimes *et al.* have investigated the degradation of polystyrene (PS) NPs using electrochemically anodized TiO_2 nanotubular layers.[11] However, the TiO_2 anatase phase has a bandgap of 3.2 eV, thereby limiting its ability to absorb only UV light, and has a faster e^-/h^+ recombination rate, which hinders the production of ($HO^\bullet$) radicals.[30] Hence, mixed anatase and rutile phases are prepared to improve e^-/h^+ separation in TiO_2 nanostructures.[37–39] Further, metal/non-metal modifications are performed on TiO_2 to improve light absorption in the visible region and promote e^-/h^+ separation, thereby improving the photocatalytic properties.[40–43] Among the dopants, Fe^{2+}/Fe^{3+} ions are quite attractive as they improve photocatalytic properties and are well known for their Fenton/photo-Fenton (PF) active properties.[40,44,45] Particularly, Fe^{2+}/Fe^{3+} undergoes a redox process with H_2O_2 to form $HO^\bullet$ radicals that decompose pollutants.[46] Ortiz *et al.* have studied the Fenton oxidation of different types of MPs, such as polyethylene terephthalate (PET), polyethylene (PE), polyvinyl chloride (PVC), polypropylene (PP), and expanded PS (EPS), as target pollutants.[47] The non-toxicity and availability of Fe make it a suitable material for the oxidation process.[44,45] Liu B. *et al.* have analyzed the degradation products of PS and nylon 6 obtained with Fe^{2+} Fenton reagents and activation with peroxymonosulfate.[48] Therefore, modification of mixed-phase TiO_2 nanostructures with Fe could be attractive for the degradation of microplastics.

In this work, peroxo-titanic acid gels synthesized by the precipitation of titanyl oxysulfate with *tert*-butylamine are freeze-dried and then subsequently annealed at 800 °C to form mixed-phase TiO_2 aerogel powders (TiAP). Further, TiAP is modified at the surface with different concentrations of Fe through the wet-impregnation technique. Therefore, the Fe-modified TiAP could exhibit both photocatalytic and photo-Fenton processes for the degradation of MPs. Indeed, Fe modification could produce additional ROS through the combination of photocatalytic and photo-Fenton processes, which could enhance the degradation of MPs. PS MPs are chosen as a model pollutant due to their ready accumulation in living organisms through respiratory, dermal, and digestive tracts.[49,50] PS is used in food packaging, toys, cup covers, storage, *etc.*,[49] therefore, it is necessary to understand effective ways to degrade PS MPs using different photo-induced processes. There are only a handful of reports on photocatalytic/Fenton-based degradation of MPs.[10,11,47] These reports deal with the evaluation of PS MP degradation through separate photocatalytic/Fenton-based processes by investigating the changes in the carbonyl and peroxyl indexes (CI/PI), mass loss after degradation, and degradation by-products.[10,11,47] However, our work investigates photocatalytic/Fenton-based degradation of PS MPs in one system using Fe-modified TiAP. Briefly, the relationship of the changes in the CI value of PS MPs with the polymer mass loss and the degradation products formed after photo-induced treatment processes are discussed. Hence, our work will bridge the knowledge gap in understanding MP degradation using photocatalytic/Fenton-based processes.

2. Materials and methods

2.1. Materials

Titanium(IV) oxysulfate ($TiOSO_4 \cdot xH_2O$, min. 29% Ti as TiO_2, Sigma-Aldrich), hydrogen peroxide (H_2O_2, aqueous solution, p.a., 30%, penta), and *tert*-butylamine (TBA, 98%, Sigma-Aldrich) were used for the preparation of TiAP. Iron(II) sulfate

heptahydrate (99% penta) was used as a precursor for Fe modification. Polystyrene beads (M_w ~192 000, Sigma Aldrich), acetone (T.G., Svero Chema), tetrahydrofuran (A.G., penta), dimethylacetamide (DMA, 99%, Sigma Aldrich), and dialysis bags (Membra-Cel™, 44 mm, MWCO-14 000, Roth) were used for the synthesis of PS MPs. Perchloric acid (68%, Lachner) and sodium hydroxide (penta) were used to adjust the pH during the photo-Fenton processes. Isopropyl alcohol (IPA, penta) and *p*-benzoquinone (BQ, ≥98%, Sigma-Aldrich) were used as scavengers during the photo-induced degradation of PS MPs.

2.2. Instrumental techniques

Crystalline phases of the prepared TiAP and Fe-modified TiAP were analyzed by X-ray diffraction (XRD, Co radiation Malvern PANalytical Empyrean III). The surface area of the photocatalysts was measured using the Brunauer–Emmett–Teller method in a Quantachrome Nova 4200e instrument. Typically, the photocatalysts were degassed at 25 °C for 72 h, and then subsequently, N_2 adsorption–desorption isotherms were measured at −196 °C. The shape and morphology of the samples were imaged using high-resolution scanning electron microscopy (HR-SEM, FEI Nova NanoSEM 450 microscope equipped with an Everhart–Thornley secondary electron detector, a through-lens detector, and an energy-dispersive X-ray analysis detector) at an accelerating voltage of 15 kV. The samples with higher and lower changes in the CI values were imaged using a high-resolution transmission electron microscope (HR-TEM, Talos F200X, Thermo Scientific, USA) with an FEG (field emission gun) operated at 200 kV, which combines scanning TEM (STEM) and TEM imaging and equipped with 4 in-column SDD Super-X windowless detectors for EDX chemical analysis and elemental mapping. Samples for HR-TEM were prepared by gently dropping a small drop of dilute (water) sample suspension on a standard TEM grid covered with carbon foil, followed by drying at ambient temperature before use. Attenuated total reflection infrared (ATR-IR) spectra were recorded by a Nicolet Nexus 670 FTIR spectrometer on a diamond crystal in the region from 400–4000 cm^{-1}. Thermogravimetric analysis (TGA) coupled with differential scanning calorimetry (DSC) and mass spectrometry (MS) were carried out to monitor the mass loss and gas evolution during the whole degradation of PS MPs. TGA-DSC-MS were performed on a NETZSCH (STA449 F1 Jupiter) instrument coupled with a gas chromatograph (GC Agilent Technologies, 7890B) and mass detector (MS Agilent Technologies, 5977B MSD). Thermoanalytical measurements were carried out in an inert atmosphere (argon, 50 cm^3 min^{-1}), in an open crucible made of α-Al_2O_3, and the initial sample mass was approx. 5 mg (crushed to fine powders). Samples were heated from 35 °C to 600 °C with a heating rate of 5 °C min^{-1}, enabling a detailed study of the decomposition process. The gaseous products were led by a heated transfer line (T = 150 °C) directly to the MS, and subsequently, gas analysis was done in SIM mode at the intensity (A) of individually selected fragments for PS, namely: m/z = 51, 78, 103, and 104. ^{1}H Nuclear magnetic resonance (NMR) spectra were recorded using a JEOL 600 MHz NMR spectrometer. All the samples were dissolved (~20 mg mL^{-1}) in d-chloroform (99.8%, Acros Organics) by sonication (several minutes) followed by centrifugation to remove the photocatalysts. Subsequently, NMR spectra of supernatant solutions were recorded. The zeta potentials were determined by laser Doppler electrophoresis using a Zetasizer Nano ZS analyzer (Malvern, UK). High-performance liquid chromatography with high-resolution mass spectrometry (HPLC-HRMS) was used to identify the by-products formed before and after the photo-induced treatment process. A description of the methodology used in the HPLC-HRMS technique is given in the ESI.†

2.3. Synthesis of microplastics

Polystyrene (PS) MPs prepared by the dialysis technique were used as a model pollutant.[51] Typically, 85 mg of PS beads were dissolved in 30 mL of organic solvent (10 mL of dimethylacetamide, 10 mL of tetrahydrofuran, and 10 mL of acetone). Later, the dissolved PS beads were poured into a dialysis bag and immersed in 1.5 L of water for 24 h, forming PS MPs. 1.5 L of water was replaced 5 times during 24 h to ensure complete removal of organic solvent. Subsequently, only the suspensions (~30 mL) of PS MPs were taken, whereas larger aggregates of the PS particles were discarded. For all photo-induced degradation processes, freshly prepared PS MP suspensions were used. The amount of PS MPs present in the suspensions after the dialysis process is approx. 30 mg (±5% error), *i.e.*, the weight is measured after centrifugation of PS MP solution followed by separating the pellets and drying at room temperature.

2.4. Synthesis of photocatalysts

2.4.1. Non-modified TiAP. TiAP are prepared by freeze-drying and subsequent annealing of peroxo-titanic acid gels formed through the precipitation of amines, according to previous report.[52] Firstly, 0.2 mol of titanium oxysulfate was dissolved in 450 mL of distilled water at 35 °C. Subsequently, the solution was cooled to 0 °C until a thin ice layer was formed. Then, *tert*-butylamine was added until pH 8 was reached, resulting in a white precipitate. Later, the white precipitate was filtered off and washed several times before resuspending in 1050 mL of distilled water. H_2O_2 was added to the suspension until pH 1–2 was reached and stirred continuously to form a transparent yellow solution of peroxo-titanic acid. The solution was stirred overnight to remove the excess H_2O_2 and finally sprayed onto liquid nitrogen before keeping in the freeze-dryer at a temperature of −64 °C and pressure of 5–10 mTorr. The obtained yellow fluffy aerogel was annealed at various rates of heating starting from 1 °C min^{-1} to 250 °C, then 2 °C min^{-1} to 500 °C, then 3 °C min^{-1} to 650 °C, and finally to 3 °C min^{-1} to 800 °C with each step lasting 1 h to form TiAP.

2.4.2. Fe-modified TiAP. Fe ions with different concentrations (0.01, 0.1, and 1 at% – $TiAP_{0.01Fe}$, $TiAP_{0.1Fe}$, $TiAP_{1Fe}$, resp.) were modified at the surface of TiAP through the wet-impregnation technique.[53] 12.5 mM TiAP were suspended in 100 mL of distilled water, followed by adding iron sulfate heptahydrate solution (1.26×10^{-6}, 1.26×10^{-5}, and 1.26×10^{-4} M) and stirred for 1 h. Later, the suspension was filtered off, dried at room temperature, and subsequently annealed at 450 °C to form different concentrations of Fe-modified TiAP. Finally, the concentration of Fe in the Fe-modified TiAP was 0.01 at%, 0.1 at%, and 1 at%, respectively, and the corresponding samples were named $TiAP_{0.01Fe}$, $TiAP_{0.1Fe}$, and $TiAP_{1Fe}$.

2.5. Photo-induced degradation experiments

The photocatalytic experiments were done using freshly prepared PS MP solution. The PS MP solution was diluted with 300 mL of water and suspended with 60 mg of photocatalyst followed by irradiation under UVA light (λ_{max} = 365 nm, 8 W, Sylvania, flux density of 6.24 mW cm^{-2} measured by UVA probe #28949; ILT 1400-A photometer) for 480 min with constant stirring and air bubbling. During the photo-induced degradation experiments, the final concentrations of PS MPs and photocatalysts were 0.1 mg mL^{-1} and 0.2 mg mL^{-1}, respectively. Photo-Fenton experiments were carried out with similar conditions to the photocatalytic process, except the pH was changed (2, 3, 5, 7, and 9), and 100 mM H_2O_2 was added every 1 h throughout the process.[54] At predetermined time intervals (0, 60, 120, 180, 240, and 480 min), 10 mL of the samples were collected and subsequently filtered to separate the solid and the liquid samples. Finally, the solid samples collected at 0 min (before treatment) and 480 min (after photocatalytic/Fenton-based processes) were analyzed by HR-SEM, HR-TEM, ATR-IR, TGA-DSC/MS, and NMR techniques. Total organic carbon content analysis (TOC, Shimadzu TNM-L ROHS) was used to quantify the organic carbon in the filtered solutions (liquid part). The sampling methodology for evaluating the PS MP degradation is given in Fig. S1.†

2.6. Evaluation of MP degradation by ATR-IR spectroscopy

The solid samples collected during the photocatalytic and photo-Fenton processes were dried at room temperature (25 °C) before analysis by ATR-IR spectroscopy. ATR-IR spectroscopy was used to calculate the CI and PI, respectively.[10] The CI and PI values indicate the oxidative degradation of MPs, *i.e.*, the cleavage of the carbonyl (1740 cm^{-1}) and peroxyl (1150 cm^{-1}) chains during the oxidation process. The CI and PI values were calculated using the following equation.

$$\mathrm{CI} = \frac{\text{Height of the peak at } 1740\ \mathrm{cm}^{-1}}{\text{Height of the reference peak at } 2850\ \mathrm{cm}^{-1}}$$

$$\mathrm{PI} = \frac{\text{Height of the peak at } 1150\ \mathrm{cm}^{-1}}{\text{Height of the reference peak at } 2850\ \mathrm{cm}^{-1}}$$

Additionally, the reference peak at 2850 cm^{-1} belongs to the C–H stretching of CH_2 groups, which is used as an internal standard to evaluate the degradation of PS MPs. Furthermore, the peak heights are normalized at 2850 cm^{-1} for optimal comparison of all the measured spectra. Importantly, values of the peak height are calculated using Gaussian fitting profiling.

3. Results and discussion

XRD patterns of TiAP and Fe-modified TiAP are shown in Fig. 1A. A mixture of TiO_2 anatase (reference code: 01-071-1166) and rutile phases (reference code: 01-072-1148) was identified for all the prepared samples. Indeed, 2θ diffraction patterns at approx. 25.33, 37.81, 48.05, 53.87, and 55.08° 2θ correspond to anatase crystal structure ((101), (004), (200), (105), and (211)), whereas 2θ diffraction patterns at approx. 27.46, 36.08, and 41.25° 2θ correspond to rutile crystal structure diffraction planes ((110), (101), and (111)). In all the samples, different compositions of anatase and rutile phases were identified and tabulated in Table 1. TiAP has 9% rutile phase, whereas Fe-modified samples $TiAP_{0.01Fe}$, $TiAP_{0.1\ Fe}$, and $TiAP_{1Fe}$ have 24%, 23%, and 13% rutile content, respectively. Mainly, Fe-modification was performed through a two-step annealing process, resulting in the development of the rutile phase during the second annealing step (Fig. S2a†). However, the increase in the Fe-content ($TiAP_{1Fe}$) stabilizes the anatase phase and inhibits rutile content formation. Nevertheless, the combined effects of anatase and rutile phases promote e^-/h^+ separation and are known to increase the photocatalytic activity.[37,38,55] Notably, mixed phases of approx. 70–90% anatase and 10–30% rutile are reported to have better photocatalytic properties.[38,39,55,56] Further, the surface area of the prepared photocatalysts was analyzed by the Brunauer–Emmett–Teller method (Fig. S2b†) and also tabulated in Table 1. TiAP had a surface area of 17.98 $m^2\ g^{-1}$, whereas Fe modification along with the two-step annealing process contributed to the slight reduction in the surface area of the samples. This minor reduction in the surface area also correlates with our other publication on similar aerogel powders with Ce modification.[53]

Fig. 1B and C show the HR-SEM images of representative TiAP and polystyrene samples. TiAP has a leaf-like morphology composed of multiple nanoparticles grouped in a structure. The average diameter of an individual nanoparticle ranges from 200 to 400 nm. Further, the PS MPs have a spherical morphology with a diameter ranging from 2 to 4.5 μm.

Before investigating the photo-induced degradation behaviour of PS MPs using non-modified TiAP and Fe-modified TiAP, they were tested with caffeine, which was used as a model organic pollutant. Since quantification of the degradation of PS MPs is not straightforward, combinations of analysis techniques such as ATR-IR spectroscopy, TOC, and TGA techniques[10,11,57] are required. For example, the degradation efficiency for pollutants, such as dyes, caffeine, pesticides, *etc.*, could be evaluated through UV-vis spectrometry, high-performance liquid

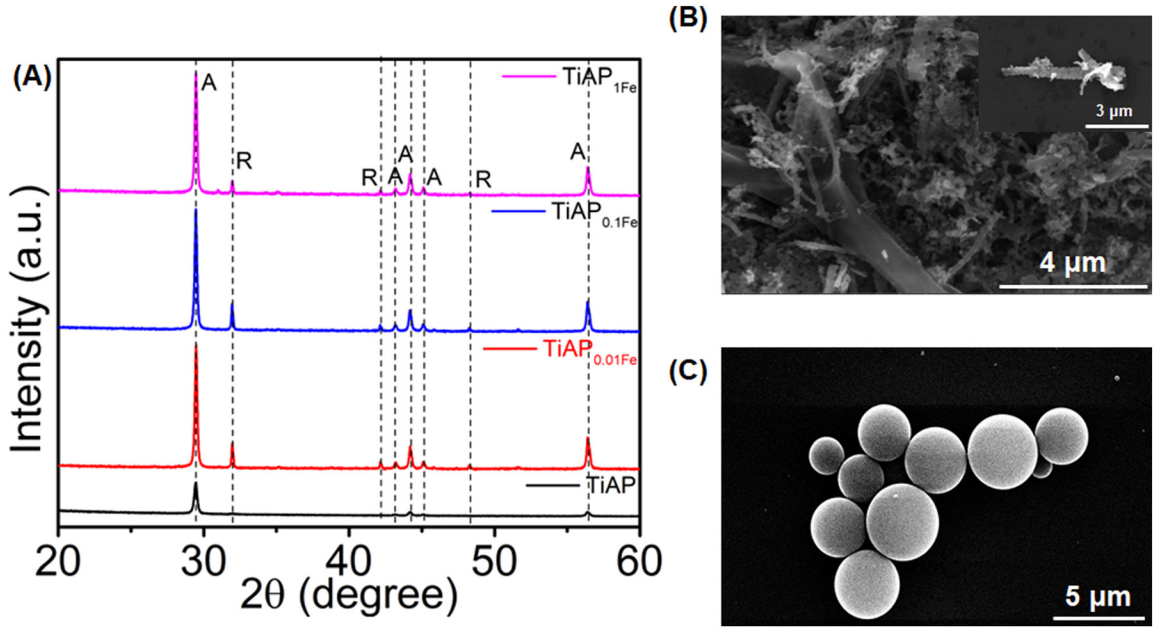

Fig. 1 (A) XRD patterns of TiAP and Fe-modified TiAP. (B) A representative HR-SEM image of TiAP and the inset shows a higher-resolution image of TiAP. (C) HR-SEM image of PS MPs taken after coating with a layer of Au–Pd.

chromatography, and TOC techniques.[10,53,58,59] Therefore, caffeine was used as a model organic pollutant to understand the degradation trend through photocatalytic and photo-Fenton-based processes using TiAP and Fe-modified TiAP (Fig. S3†). Accordingly, $TiAP_{0.1Fe}$ showed the highest caffeine degradation extent in photocatalytic (~45%) and photo-Fenton-based processes (~99%) after 120 min of UVA light irradiation. Hence, photo-induced degradation of PS MPs was discussed in detail for TiAP and $TiAP_{0.1Fe}$.

Firstly, the photo-induced degradation of PS MPs (solid samples) was monitored by ATR-IR spectroscopy by monitoring the changes in the carbonyl and peroxyl groups (Fig. S4 and S5†). Noticeably, the oxidation reaction leads to chain scission, cross-linking, and discoloration of PS MPs.[60] The oxidation reaction in PS compounds occurs due to the formation of HO$^{\bullet}$, ROO$^{\bullet}$ (peroxyl radical), and POO$^{\bullet}$ (polystyryl radicals).[60,61] The POO$^{\bullet}$ radicals that exist in an excited state are converted to ROO$^{\bullet}$ radicals under reaction with oxygen.[27,61] HO$^{\bullet}$ radicals and ROO$^{\bullet}$ radicals are responsible for chain scission of the polymers that increase the CI.[10,27,61]

Table 1 The composition of the anatase phase, crystallite size, and surface area of TiAP and all concentrations of Fe-modified TiAP were tabulated

Sample	Anatase (%)	Anatase crystallite size (nm)	Surface area ($m^2\ g^{-1}$)
TiAP	91	51.4	17.98
$TiAP_{0.01Fe}$	76	51.9	10.49
$TiAP_{0.1Fe}$	77	76.7	11.51
$TiAP_{1Fe}$	87	56.5	17.58
TiAP_2 step annealed	74	56.3	12.23

The degradation of PS MPs occurs in multidirectional pathways, leading to the formation of multiple polymer moieties and various intermediates.[61] Eventually, the end products of the PS MP degradation in all the pathways are CO_2 and H_2O.[10,11] Possible pathways for photo-induced oxidation (photocatalytic and photo-Fenton processes) using TiO_2 structures (TiAP and Fe-modified TiAP) of PS MPs are given below.[10,61]

$$TiO_2 + O_2 + e^- (h\nu) \rightarrow O_2^{\bullet -}$$

$$TiO_2 + H_2O + h^+ (h\nu) \rightarrow HO^{\bullet} + H^+$$

HO$^{\bullet}$ radicals produced from the photocatalytic and photo-Fenton processes cause polymer chain scission.[10,61] Apart, from TiO_2, photolysis of H_2O_2 also produces the HO$^{\bullet}$ radicals.[27,62]

$$HO^{\bullet} + \sim CH_2CHPh - CH_2\sim \rightarrow \sim CH_2C^{\bullet}\ PhCH_2\sim \text{ (macro-radical)} + H_2O$$

$$HO^{\bullet} + \sim CH_2CHPh - CH_2\sim \rightarrow \sim C^{\bullet}\ HCHPhCH_2\sim + H_2O$$

Macro-radicals are also formed during the photodegradation of PS under UV irradiation, leading to polymer chain scissions.[61] These macro radicals react with oxygen to form peroxyl radicals or hydroperoxide compounds.

$$\sim CH_2C^{\bullet}\ PhCH_2\sim + O_2 \rightarrow \sim CH_2C(O_2^{\bullet})PhCH_2\sim \text{ (peroxyl radical)}$$

$$\sim CH_2C^{\bullet}\,PhCH_2\sim + O_2 \rightarrow \sim CH_2C(OOH)PhCH_2\sim \text{ (hydroperoxide)}$$

$$\sim CH_2C(O_2^{\bullet})PhCH_2\sim + h\nu \rightarrow \sim CH_2C(O^{\bullet})PhCH_2\sim \text{ (alkoxyl radical)}$$

$$\sim CH_2C(O^{\bullet})PhCH_2\sim + \sim CHPh\sim \text{ (neighbouring moeity)} \rightarrow \sim CH_2C(OH)PhCH_2\sim$$

$$\sim CH_2C(O^{\bullet})PhCH_2\sim \rightarrow \sim CH_2C(O)CH_2\sim + Ph^{\bullet}$$

$$\sim CH_2C(O^{\bullet})PhCH_2\sim \rightarrow \sim CH_2C(O)Ph\sim + \sim C^{\bullet}H_2 - CHPh\sim$$

The chain scission of PS MPs during the photo-induced oxidation process will form multiple polymer moieties that could influence the changes in the carbonyl and peroxyl groups in the ATR-IR spectra. The CI and PI values were calculated using the ratio changes in carbonyl (at 1740 cm^{-1}) and peroxyl groups (at 1150 cm^{-1}) in comparison to internal standards (reference group of C–H stretching of the $-CH_2-$ group) at 2850 cm^{-1}.[10] Therefore, the CI and PI value changes indicate the oxidative degradation of PS MPs. Relative changes in CI and PI were calculated with respect to the non-treated samples (Fig. 2A and Table S1†). The photocatalytic process by TiAP showed approx. 26% increase in CI and a 38% decrease in PI values, whereas TiAP with H_2O_2 showed approx. 52% and 39% increase in CI and PI values, respectively. The decrease in PI could indicate that the degradation did not occur in the direction of forming peroxyl-containing moieties; instead, peroxyl radicals are eventually converted to alkoxyl radicals that form carbonyl groups. Notably, Fe-modified TiAP samples show different changes in CI and PI values for photocatalytic and photo-Fenton processes. For instance, photocatalytic and photo-Fenton processes with $TiAP_{0.01Fe}$ and $TiAP_{1Fe}$ showed a decreased CI and increased PI value. This implies that one of the PS degradation pathways is due to the formation of the peroxyl group. Additionally, the decrease in CI could indicate another pathway of PS degradation, *i.e.*, based on the Norrish-I mechanism that forms carbon monoxide during the photo-induced degradation process.[63–65] Ghanadi *et al.*[64] reported a decrease in the CI value for the HDPE polymer observed after the first few days of exposure to UV radiation. $TiAP_{0.1Fe}$ showed the highest CI and PI values, increasing to approximately 36% and 58% for the photocatalytic and photo-Fenton processes, respectively.

To further solidify the versatility of Fe modification on TiAP, especially for the photo-Fenton-based degradation of PS MPs, the homogenous photo-Fenton process containing Fe^{2+} ions was carried out at different pH values (2, 3, 5, 7, and 9). Equivalent concentrations of Fe^{2+} present (~12.6 μM Fe^{2+} salt) in $TiAP_{0.1Fe}$ were used for the homogenous Fenton process. Accordingly, higher changes in CI and PI values were observed for the $TiAP_{0.1Fe}$ system in all tested pH ranges (Fig. S6†). Therefore, it's evident that the presence of TiAP along with Fe^{2+} assists in the efficient degradation of PS MPs. Moreover, at pH 2, both CI and PI values had higher changes. Notably, the calculations of CI and PI through carbonyl and peroxyl groups are only semi-quantitative methods for analyzing the polymer oxidation process.[10] Hence, additional methodologies are required to quantify PS degradation efficiency. Fig. 2B shows the carbon content monitored throughout the PS degradation (liquid part) process for all the samples. The liquids collected for TOC analysis showed an increasing carbon content throughout the reaction. The photocatalytic process with $TiAP_{0.1Fe}$ showed the highest increase in the carbon content. Typically, the detection of higher carbon content in the liquid part is due to the release of carbon chains during the polymer photo-degradation process. A representative liquid part (TiAP_PC) collected after

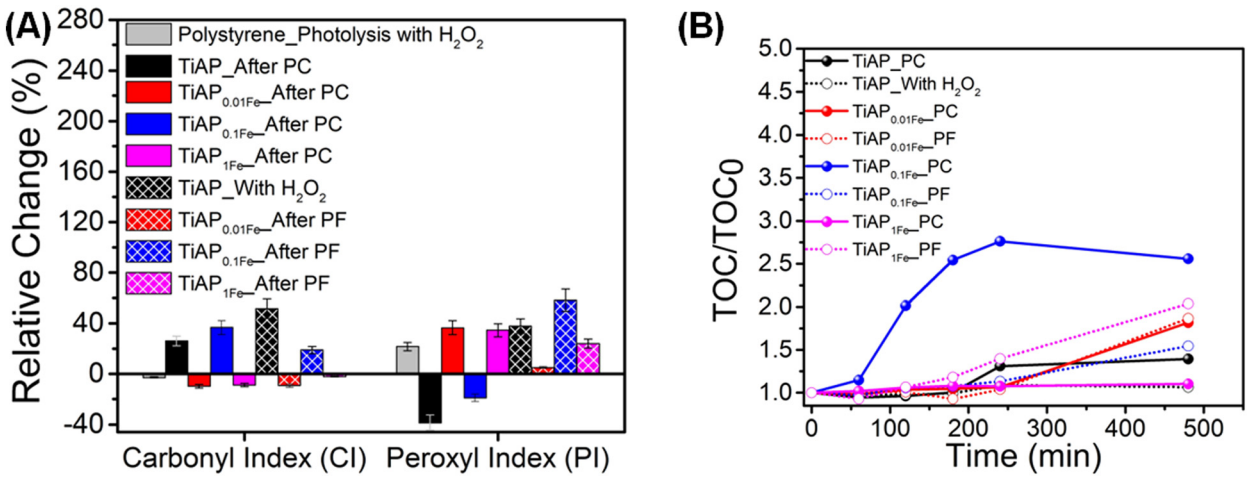

Fig. 2 (A) Relative changes in the CI and PI after the photocatalytic (PC) and photo-Fenton (PF)-based processes for TiAP and different concentrations of Fe-modified TiAP. (B) TOC was monitored throughout the PC and PF processes.

480 min and 24 h of irradiation was analyzed by NMR, and proton signals between 0.8 and 1.9 ppm belonging to aliphatic groups were observed (Fig. S7a†). Therefore, ROS generated during the photocatalytic degradation were used to break the PS MPs into aliphatic chains. However, with prolonged irradiation (at least 24 h), the broken polymer chains eventually mineralized to CO_2 and H_2O.[10,11] Indeed, the longer irradiation time (24 h) using TiAP resulted in approx. 53% mineralization of the PS MPs (Fig. S7b†). Since this work deals with understanding the photocatalytic/Fenton processes in non-modified and Fe-modified TiAP, the TOC experiments were not carried out for a longer treatment time for other samples. The summaries of reported research work on CI, PI, and mineralization extent according to their photocatalytic conditions are tabulated in Table S2.† Our reported CI, PI, and mineralization extent are similar to other reported studies on the photo-induced degradation of PS MPs.

HR-SEM and HR-TEM images before the treatment and after the photocatalytic and photo-Fenton-based process are shown in Fig. 3 and 4 and S8,† respectively. The representative EDX mapping in Fig. 3B shows that the spherical-shaped particles are carbon (green) belonging to the PS MPs, and Ti (red) covers the surface of PS MPs. O (white) is present throughout the samples that belong to PS MPs and TiO_2 photocatalysts. Interestingly, after 480 min of both photocatalytic/Fenton-based processes, the photocatalyst (TiAP and Fe-modified TiAP) covers the surface of the PS MPs. This coverage of the photocatalysts around the PS MPs could facilitate an attack of the HO˙ radicals on the PS MPs, leading to their degradation.[61]

The thermal decomposition of the PS MPs before and after the photo-induced processes using non-modified TiAP, $TiAP_{0.01Fe}$, and $TiAP_{0.1Fe}$ was investigated using TGA/DSC-MS (Table 2, Fig. S9–S11†). Particularly, the mass loss was recorded for the samples with the highest and lowest changes in CI value (Fig. 2A). Further, the thermal decomposition of unmodified peroxo-titanate powders without PS MPs was investigated in detail in our previous study.[52,66,67] Evidently, all the samples before and after the photo-induced processes showed two-step thermal decomposition. In the first step, between 30 and 200 °C, the evolution of adsorbed water from the surface of the samples was observed. Then, in the second step, the decomposition of PS MPs with a DTG curve maximum at approx. 440 °C was observed to be connected with the evolution of PS fragments with m/z of 51, 78, 103, and 104.[68,69] Further, hardly any changes in the DSC curve were observed during the measurements (Fig. S9–S11†). The glass transition temperature of PS was hardly observed around 100 °C[70] because of the simultaneous thermal analysis measurements. Also, there are the same changes around the temperature of the main degradation step, which is approx. at 440 °C. The mass residue is 53–68% for the measured samples, *i.e.*, around 32–47% of the

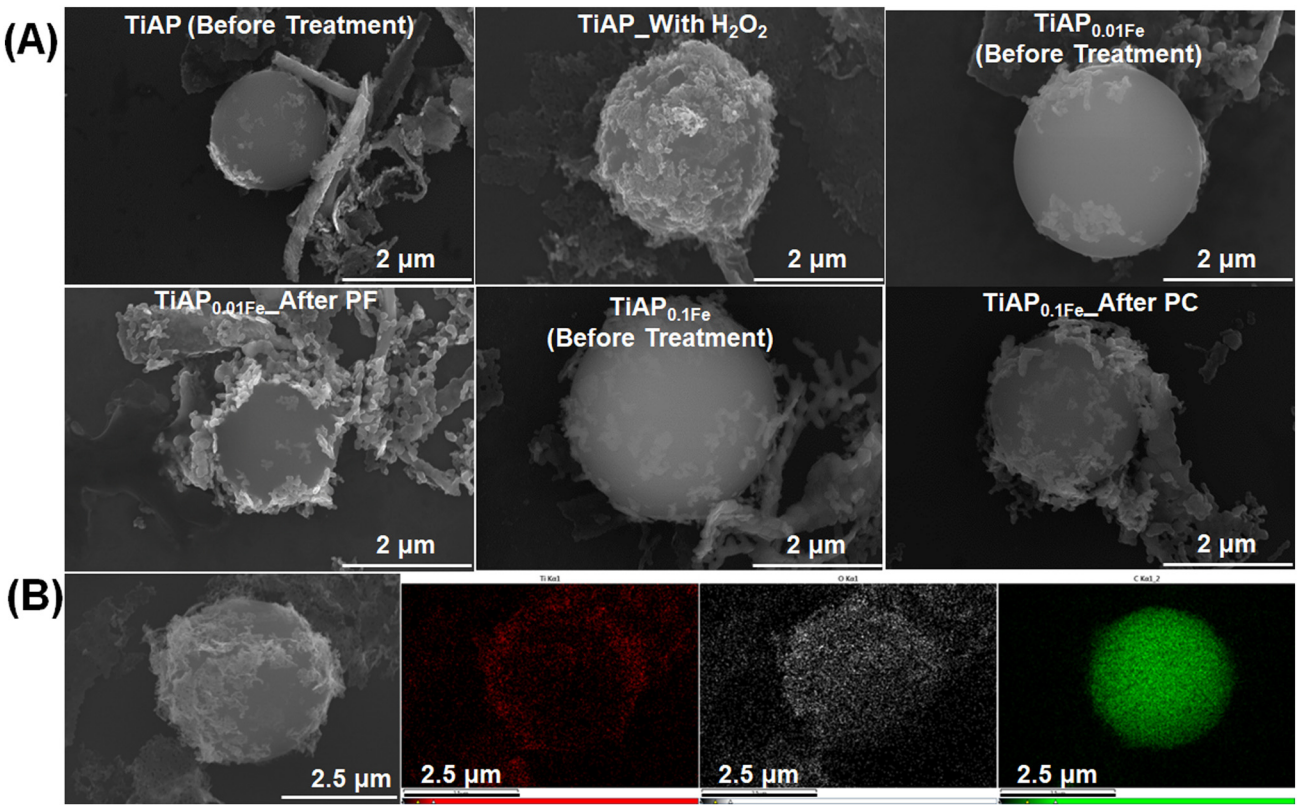

Fig. 3 (A) Representative HRSEM images before treatment and samples with a higher change in CI value after the photo-induced treatment process and (B) EDX mapping of the representative sample (TiAP_Before Treatment), showing the distribution of C (PS MPs) colored in green, Ti in red, and O in white.

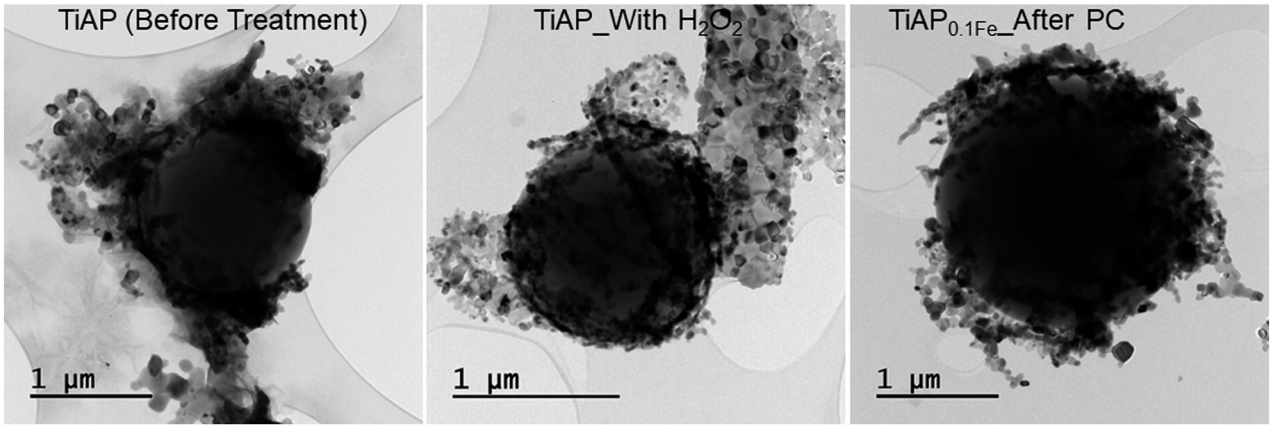

Fig. 4 Representative HR-TEM images of TiAP before treatment and samples with higher changes in the CI value (TiAP_With H_2O_2 and $TiAP_{0.1Fe}$_After PC).

PS MPs were released during the thermal decomposition process. However, it could be observed that there is a clear difference in the total mass residue for the samples with the highest change in the CI value (TiAP_With H_2O_2 and $TiAP_{0.1Fe}$_After PC). For instance, before the treatment, non-modified TiAP and $TiAP_{0.1Fe}$ had retained approx. 61% and 56% of their initial mass, respectively. However, after the photo-induced treatment process, the mass residue increased to approx. 68% for TiAP_With H_2O_2 and 65% for $TiAP_{0.1Fe}$_After PC. Since PS MPs were already degraded during the photo-induced treatment process, there is a higher mass residue for the samples with higher changes in the CI value. In other words, PS MPs were partially removed during the photo-degradation process, and a higher percentage of the materials' mass belongs to the photocatalysts (TiAP or Fe-modified TiAP). I. Nabi *et al.*[57] also showed that in the case of PS MP-modified TiO_2 films, 100% of the material mass belongs to TiO_2 after the photocatalytic treatment. Additionally, the samples with lower changes in CI value ($TiAP_{0.01Fe}$_After PF and $TiAP_{0.1Fe}$_After PF) showed no significant differences in the total mass residue before and after the photo-induced treatment process (Table 2 and Fig. S11†). Furthermore, the samples with higher changes in the PI values ($TiAP_{0.1Fe}$_After PF) did not affect the mass residue in the TGA/DSC-MS spectra. Hence, it could be understood that the changes in the CI values are necessary to affect the mass residue after the photo-induced treatment process. Importantly, to confirm the reproducibility of the experiments, TGA/DSC-MS measurements were repeated 5 times for a representative sample (TiAP_With H_2O_2), and the differences between particular measurements were ±2.10%. Therefore, the chosen evaluation methodology can be considered reliable due to the negligible error in TGA-DSC/MS measurements.

Table 2 TGA/DSC-MS results of the temperature onset of the main degradation step (T_{onset}) and the mass residue at 600 °C ($R_{600°C}$) before and after the photo-induced treatment process

Sample	T_{onset} (°C)	$R_{600°C}$ (%)
TiAP (before treatment)	400	60.81
TiAP_With H_2O_2	407	67.90
$TiAP_{0.1Fe}$ (before treatment)	414	56.36
$TiAP_{0.1Fe}$_After PC	419	64.70
$TiAP_{0.1Fe}$_After PF	416	53.05

Interestingly, preliminary studies showed that the photo-Fenton-based process using $TiAP_{0.1Fe}$ showed the highest caffeine degradation efficiency among all the treated samples. However, a similar degradation efficiency in the photo-Fenton process could not be obtained for PS MPs. This could be because the mechanism of caffeine and PS MP adsorption onto the photocatalysts differs between these two pollutants. For instance, zeta potential measurements (Fig. S12†) showed that the surface charge of caffeine at acidic pH (~3) and near neutral pH (~6) is close to zero.[71–73] Further, the surface charge of Fe-modified TiO_2 (TiAP and Fe-modified TiAP) remains positive for both neutral and acidic pH, respectively.[74] During the photo-induced degradation process in water, the caffeine molecule adsorbs onto TiO_2 (TiAP and Fe-modified TiAP) through hydrogen bond formation.[75,76] Therefore, caffeine degradation is better for photocatalytic and photo-Fenton processes using TiAP and Fe-modified TiAP. However, the surface charge of PS MPs changes at near neutral and acidic pH. Zeta potential measurements (Fig. S12a†) showed that the surface charge of PS MPs at near neutral and acidic pH is negative and positive, respectively.[71,72] Hence, owing to the better electrostatic interaction between PS MPs and photocatalysts (TiAP and TiAP-Fe) at near neutral pH a higher degradation efficiency is exhibited. Meanwhile, at acidic pH, both photocatalysts and PS MPs showed positive surface charges, and hence, the interaction between them became weaker, thereby affecting the degradation efficiency. To confirm the interaction of a positively charged photocatalyst with another positively charged pollutant, methylene blue (MB) was chosen as a model organic cationic pollutant.[77] Interestingly, almost similar MB degradation efficiency (~61%) was obtained between photocatalytic and photo-Fenton processes at acidic pH using $TiAP_{0.1Fe}$ (Fig. S12b†). This indicates that

electrostatic repulsion inhibits the photo-Fenton degradation process at acidic pH. Indeed, the degradation efficiency is related to the surface charge of the pollutant and the photocatalyst.[58,77] Nevertheless, $TiAP_{0.1Fe}$ showed good photocatalytic degradation of PS MPs among all the tested samples. Even though the photo-Fenton process was weaker, it still exhibited oxidative degradation of PS MPs.

Proton NMR spectra were recorded for the as-prepared PS MPs, TiAP_With H_2O_2, and $TiAP_{0.01Fe}$_After PF (Fig. 5). Typically, as-prepared PS MPs prepared for this study have one set of peaks between 6.3 and 7.2 ppm belonging to aromatic protons of the styrene moiety and between 0.8 and 1.9 ppm belonging to aliphatic protons.[78] Already, oxidized moieties of aromatic alcohols are present in the as-prepared PS MPs at 2.3 and 5 ppm.[78] During the photo-induced degradation, polymer chains undergo scissions, which could be observed in the NMR spectrum. Indeed, new NMR peaks formed for TiAP_With H_2O_2 and $TiAP_{0.01Fe}$_After PF, especially at 0.82 and 1.27 ppm (Fig. 5B and C). Furthermore, during the photo-induced oxidation process, the cleavage of aliphatic and aromatic alcohol groups, *i.e.*, the peaks at 1.83, 2.26, and 5.01 ppm, was absent in the treated samples. Additionally, proton NMR spectra recorded for the homogenous Fenton process using Fe^{2+} at pH 2 and pH 9 (Fig. S13†) revealed only the formation of new peaks of aliphatic protons (at 0.83 and 1.28 ppm). In contrast, negligible changes occurred in aliphatic and aromatic alcohol groups. This difference in NMR spectra also could indicate that these polymer chains were only partially affected during the homogenous photo-Fenton degradation process. Importantly, NMR spectra could be used to identify the oxidative degradation of the PS MPs but not to determine the extent of the degradation efficiency. Therefore, the samples, irrespective of their degradation efficiency, showed the oxidation of the polymer chains in the PS MPs.

Complementary to NMR spectra, HPLC-HRMS confirmed the oxidation of PS MPs through photo-induced processes (Fig. 6 and S14 and S15†). HPLC-HRMS measurements were carried out in both negative and positive modes for non-treated PS MPs and samples with the highest change in CI value (TiAP_With H_2O_2). Interestingly, the spectra for PS MPs and TiAP_With H_2O_2 could be obtained only from the negative mode, indicating that by-products are polar compounds that ionize by deprotonation. Further, clear differences in chromatogram profiles were observed for PS MPs and TiAP_With H_2O_2, at the wavelength of 220 nm and 280 nm, thereby confirming the photo-induced oxidation of PS MPs (Fig. S14 and S15†). Additionally, the *m*/*z* spectrum showed the formation of additional peaks, which could be possibly due to the degradation of PS MPs (Fig. 6). The *m*/*z* at

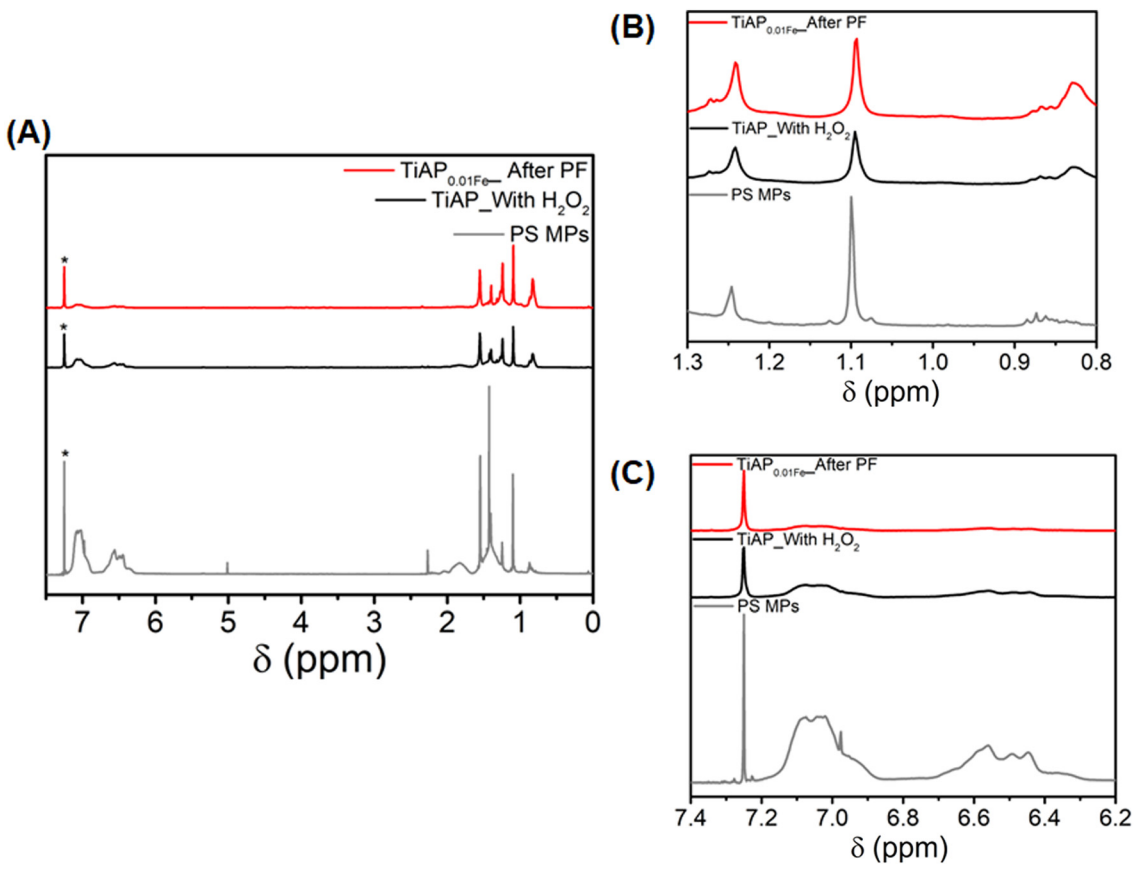

Fig. 5 (A) ^{1}H NMR spectra of PS MPs, TiAP_With H_2O_2, and $TiAP_{0.01Fe}$_After PF. (B) and (C) The zoomed-in spectra between 0.8–1.3 ppm and 6.2–7.5 ppm, respectively. Solvent peaks are marked with an asterisk (*).

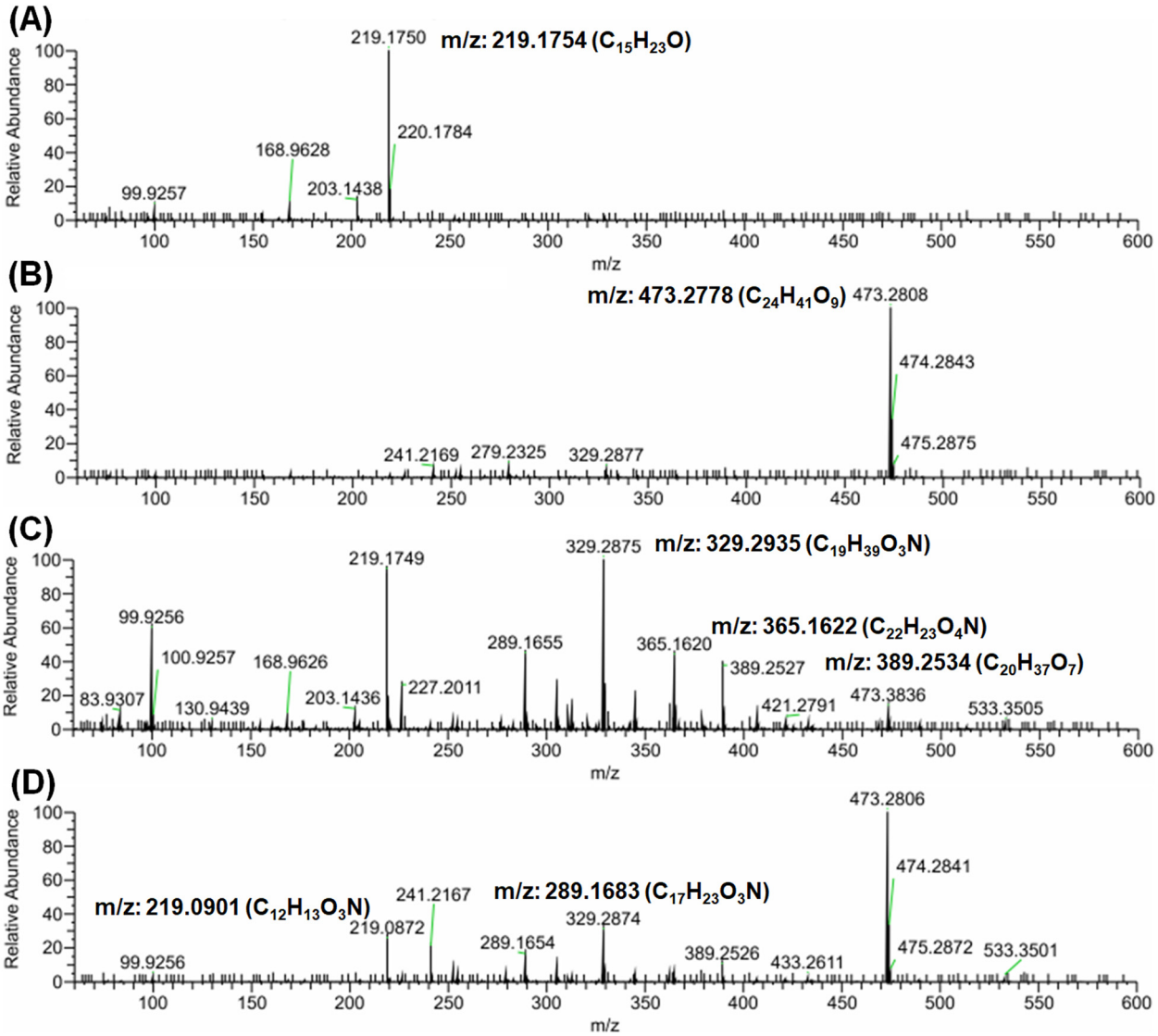

Fig. 6 HRMS spectra of (A and B) PS MPs zoomed in at retention times of 16.64 and 17.27, respectively. (C and D) TiAP_With H_2O_2 zoomed in at retention time of 16.72 and 17.33, respectively. Spectra were taken at a fragmentation intensity of 70 V.

219, 289, 329, 365, and 389 are closely related to the phenyl groups, esters, and organic acids, which are common oxidative degradation by-products.[10,11] Based on *m*/*z*, plausible intermediates formed are shown in Fig. S16.† Therefore, the formation of degradation by-products confirms the photo-induced degradation of PS MPs.

The main ROS responsible for the degradation of PS MPs during the photoinduced degradation process using $TiAP_{0.1Fe}$ were determined by electron paramagnetic resonance (EPR) spectroscopy. The EPR spin trapping technique utilizing 5,5-dimethyl-1-pyrroline *N*-oxide (DMPO) was used to identify the transient paramagnetic species formed upon exposure of the aerated dispersions of $TiAP_{0.1Fe}$. The immediate formation of the characteristic 4-line signal upon LED@365 nm exposure, assigned to the $^{\bullet}$DMPO–OH spin-adduct with spin-Hamiltonian parameters (a_N = 1.501 mT, a_H^{β} = 1.477 mT, $a_{13C}(6x^{13}C)$ = 0.737 mT, g = 2.0057; Fig. 7A) in the reaction system $TiAP_{0.1Fe}$/DMPO/water, was observed. The spin-adduct represents the HO$^{\bullet}$ formed upon (*i*) oxidation of HO^-/H_2O adsorbed on the photocatalyst's surface and (*ii*) cascade complex reactions *via* $O_2^{\bullet-}/H_2O_2$ trapped by the DMPO spin trap.[79,80] The dominant pathway – genuine spin trapping – was supported by adding an aprotic dimethylsulfoxide (DMSO) solvent into an aqueous suspension of $TiAP_{0.1Fe}$ (20% vol. DMSO). The LED@365 nm exposure led to the generation of two spin-adducts, and the 6-line signal was attributed to carbon-centered $^{\bullet}$DMPO–CH_3 (a_N = 1.325 mT, a_H^{β} = 2.320 mT, g = 2.0057, c_{rel} = 65%) along with $^{\bullet}$DMPO–OH (a_N = 1.495 mT, a_H^{β} = 1.442 mT, g = 2.0057, c_{rel} = 35%; data not shown). The rapid reaction of HO$^{\bullet}$ with DMSO produces methyl radicals, detectable in the reaction with DMPO as the corresponding spin-adduct $^{\bullet}$DMPO–CH_3. The rapid dismutation of the superoxide radical anion and low stability of $^{\bullet}$DMPO–O_2^-/OOH in water limit the detection of $O_2^{\bullet-}$ in an

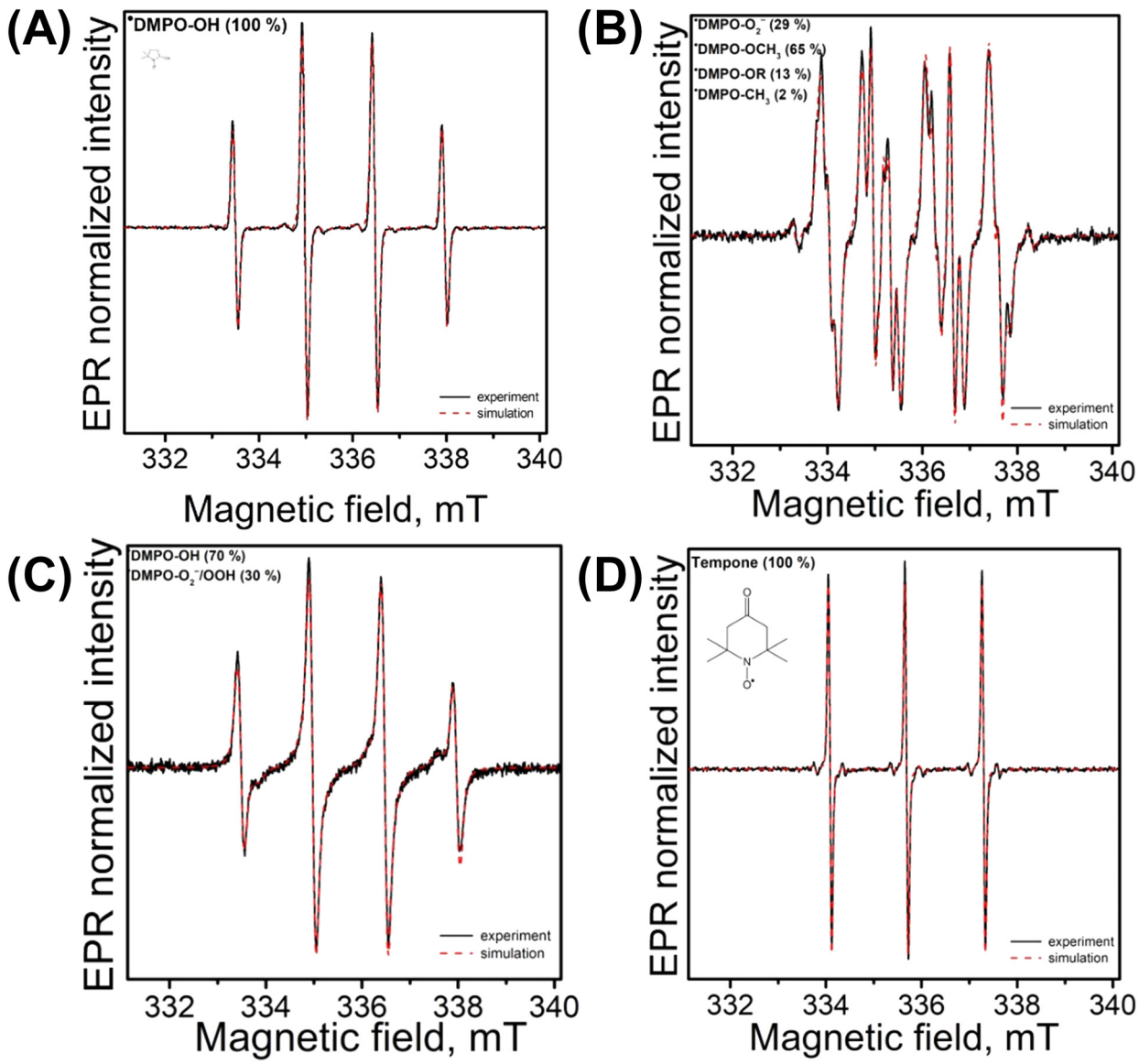

Fig. 7 Experimental (black) and simulated (red) EPR spectra (SW = 9 mT) obtained upon LED@365 nm exposure (irradiance 17 mW cm^{-2}; exposure 300 s) of the aerated $TiAP_{0.1Fe}$ suspensions in the presence of (A) spin trap DMPO in water, (B) spin trap DMPO in DMSO, (C) spin trap DMPO in water in the presence of H_2O_2 (0.7% vol.) and (D) sterically hindered amine TMPO in water ($TiAP_{0.1Fe}$ concentration 0.2 mg mL^{-1}; $c_{0,DMPO}$ = 0.042 M; $c_{0,TMPO}$ = 0.010 M).

aqueous environment. To support its formation upon exposure, the experiments were performed in DMSO, a well-known solvent stabilizing the superoxide radical anions.[79] The LED@365 nm exposure of the aerated DMSO suspension of $TiAP_{0.1Fe}$ in the presence of DMPO resulted in the generation of four spin-adducts (Fig. 7B): $^{\bullet}DMPO\text{–}O_2^-$ (a_N = 1.287 mT, a_H^β = 1.037 mT, a_H^γ = 0.140 mT, g = 2.0057, c_{rel} = 29%) produced by the reaction of $O_2^{\bullet-}$ with DMPO and $^{\bullet}DMPO\text{–}OCH_3$ (a_N = 1.329 mT, a_H^β = 0.799 mT, a_H^γ = 0.162 mT, g = 2.0057, c_{rel} = 56%), $^{\bullet}DMPO\text{–}OR$ (a_N = 1.390 mT, a_H^β = 1.162 mT, g = 2.0057, c_{rel} = 13%), and $^{\bullet}DMPO\text{–}CH_3$ (a_N = 1.438 mT, a_H^β = 2.127 mT, g = 2.0057, c_{rel} = 2%).[79,80] The production of the $^{\bullet}DMPO\text{–}OCH_3$ adduct is initiated by generated ROS (mainly $HO^{\bullet}$), which immediately attack the DMSO molecules, forming methyl radicals, and the rapid reaction of these methyl radicals with molecular oxygen results in the generation of peroxomethyl radicals serving as a source of $^{\bullet}DMPO\text{–}OCH_3$ spin-adducts. The main source of ROS is adsorbed H_2O/HO^- naturally occurring on the photocatalyst surface.[79,80]

The addition of H_2O_2 to the aerated aqueous suspension of $TiAP_{0.1Fe}$ in the presence of DMPO upon LED@365 nm exposure resulted in the generation of two EPR signals assigned to $^{\bullet}DMPO\text{–}OH$ (c_{rel} = 70%) and $^{\bullet}DMPO\text{–}O_2^-/OOH$ (a_N = 1.456 mT, a_H^β = 1.129 mT, a_H^γ = 0.158 mT, g = 2.0057, c_{rel} = 30%) (Fig. 7C). The presence of the second-mentioned spin-adduct in aqueous media is relatively scarce; under given experimental conditions, $HOO^{\bullet}$ is formed, and the oxidation/

reduction of H_2O_2 by photogenerated holes and electrons leads to the effective formation of molecular oxygen.[81] The higher amount of molecular oxygen was evidenced by the presence of small bubbles in the EPR quartz cell and broadened lines of EPR signals were observed. The higher concentration of O_2 (and consecutive formation of $O_2^{\bullet-}$) and the occurrence of HOO$^\bullet$ enable the more effective generation of the $^\bullet$DMPO–O_2^-/OOH spin-adduct.[82] It should be noted here that an analogous experiment without a photocatalyst in the reaction system resulted only in the formation of $^\bullet$DMPO–OH, and no presence of other spin-adducts was found.

The photoinduced oxidation of sterically hindered amines, *e.g.*, 4-oxo-2,2,6,6-tetramethylpiperide *N*-oxyl (TMPO), leads to the formation of stable free nitroxide 4-oxo-2,2,6,6-tetramethylpiperidone (Tempone). Fig. 7D represents experimental and simulated EPR spectra of stable free nitroxide Tempone formed upon LED@365 nm exposure in the reaction system $TiAP_{0.1Fe}$/TMPO/water/air (a_N = 1.611 mT, $a_{13C}(6x^{13}C)$ = 0.641 mT, g = 2.0055). The main species responsible for the oxidation is singlet oxygen ($^1O_2$), however, ROS or other reactive species should be considered.[79] The addition of sodium azide, a widely used water-soluble $^1O_2$ quencher,[79] led to a significant drop in EPR signal intensity (80% decrease), supporting the $^1O_2$ formation under experimental conditions. Additionally, the formation of the ROS during the photo-induced degradation process was complemented by scavenging experiments. IPA (HO$^\bullet$)[53,83] and BQ ($O_2^{\bullet-}$ and $^1O_2$)[53,84,85] were used as scavengers for photocatalytic and photo-Fenton degradation processes, respectively (Fig. S17a†). The presence of both IPA and BQ reduced the changes in the CI and PI values during the photo-catalytic/Fenton process using $TiAP_{0.1Fe}$, thereby confirming the generation of these ROS (HO$^\bullet$, $O_2^{\bullet-}$, and $^1O_2$) in both the photocatalytic and photo-Fenton systems. Additionally, probably due to the quenching effect of the scavenger, proton NMR spectra (Fig. S17b†) also showed only the formation of new peaks at 0.83 and 1.28 ppm, whereas no changes in the aromatic and aliphatic alcohol groups were observed. Therefore, modification of TiAP with Fe produces ROS by both the photocatalytic and photo-Fenton processes, thereby enhancing the degradation efficiency of PS MPs (Fig. S18†). The ROS cleave polystyrene into intermediates (detected by HPLC-HRMS) which finally mineralize into CO_2 and H_2O. This work will eventually lead to an understanding of using efficient nanostructures to study the degradation of PS MPs in the environment.

Conclusions

TiO_2 nanostructures were successfully prepared as aerogel powders and further modified at the surface with Fe for photocatalytic and photo-Fenton-based PS MP degradation. The changes in CI and PI values corresponding to the photo-induced degradation of PS MPs were observed with TiAP, and Fe-modified TiAP (0.01–1 at%) were monitored by ATR-IR spectroscopy technique. Accordingly, TiAP_With H_2O_2 and $TiAP_{0.1Fe}$_After PC showed the highest change in the CI value, *i.e.*, these two samples exhibited the highest degradation of PS MPs. Owing to the better electrostatic interaction between the PS MPs and catalyst (TiAP and $TiAP_{0.1\ Fe}$) a higher degradation efficiency was achieved. In contrast, in the photo-Fenton-based system, the electrostatic interaction between PS MPs and Fe-modified TiAP ($TiAP_{0.1Fe}$) became weaker, lowering the degradation efficiency. Even though Fe modification improves e^-/h^+ separation, the electrostatic interaction between the pollutant and catalyst plays a vital role in the degradation of organic pollutants. Further, TGA/DSC-MS showed that the samples with higher CI value changes showed significant residual mass changes after the photo-induced treatment process. In contrast, samples with lower changes in the CI value did not trigger a residual mass change. Subsequently, NMR spectral peaks related to the oxidative degradation of PS MPs were observed for the samples with higher and lower changes in the CI values, confirming the breakage of the polymer chains. Furthermore, HPLC-HRMS spectra showed the formation of degradation by-products after the photo-induced degradation process for the sample with a higher change in the CI value. Finally, TOC results for more extended treatment time revealed the eventual mineralization of the PS MPs. EPR spectroscopy and scavenging experiments show the generation of ROS in photocatalytic (HO$^\bullet$, $O_2^{\bullet-}$, and $^1O_2$) and photo-Fenton (HO$^\bullet$, HOO$^\bullet$, and $O_2^{\bullet-}$) systems using $TiAP_{0.1Fe}$. This study will assist in preparing efficient nanostructures and choosing better photo-induced processes for treating MPs in water.

Data availability

The data supporting this article have been included as part of the ESI.†

Author contributions

Guru Karthikeyan Thirunavukkarasu: conceptualization, investigation, methodology, visualization, writing-original draft, writing-review & editing. Monika Motlochová: methodology, visualization, writing-review & editing. Dmytro Bavol: investigation, methodology, writing-review & editing. Anna Vykydalová: investigation, methodology, writing-review & editing. Jaroslav Kupčík: investigation, methodology, writing-review & editing. Michal Navrátil: investigation, methodology, writing-review & editing. Kaplan Kirakci: methodology, writing-review & editing. Eva Pližingrová: methodology, writing-review & editing. Dana Dvoranová: investigation, methodology, writing-review & editing. Jan Šubrt: investigation, methodology, writing-review & editing.

Conflicts of interest

There are no conflicts to declare.

Acknowledgements

This work was supported by i) Research Infrastructure NanoEnviCz, supported by the Ministry of Education, Youth and Sports of the Czech Republic under Project No. LM2018124 and ii) Programme to Support Prospective Human Resources – post Ph.D. candidates from the Czech Academy of Sciences under project no: L200322301. This work was partially financially supported by Scientific Grant Agency of the Slovak Republic (Project VEGA 1/0422/24) (Dana Dvoranová).

Notes and references

1 L. M. Heidbreder, I. Bablok, S. Drews and C. Menzel, Tackling the plastic problem: A review on perceptions, behaviors, and interventions, *Sci. Total Environ.*, 2019, **668**, 1077–1093.
2 P. Dauvergne, Why is the global governance of plastic failing the oceans?, *Global Environ. Change*, 2018, **51**, 22–31.
3 D. K. A. Barnes, F. Galgani, R. C. Thompson and M. Barlaz, Accumulation and fragmentation of plastic debris in global environments, *Philos. Trans. R. Soc., B*, 2009, **364**, 1985–1998.
4 J. R. Jambeck, R. Geyer, C. Wilcox, T. R. Siegler, M. Perryman, A. Andrady, R. Narayan and K. L. Law, Plastic waste inputs from land into the ocean, *Science*, 2015, **347**, 768–771.
5 J. O. Babayemi, I. C. Nnorom, O. Osibanjo and R. Weber, Ensuring sustainability in plastics use in Africa: consumption, waste generation, and projections, *Environ. Sci. Eur.*, 2019, **31**, 60.
6 B. R. Kiran, H. Kopperi and S. Venkata Mohan, Micro/nano-plastics occurrence, identification, risk analysis and mitigation: challenges and perspectives, *Rev. Environ. Sci. Biotechnol.*, 2022, **21**, 169–203.
7 S.-A. Strungaru, R. Jijie, M. Nicoara, G. Plavan and C. Faggio, Micro- (nano) plastics in freshwater ecosystems: Abundance, toxicological impact and quantification methodology, *TrAC, Trends Anal. Chem.*, 2019, **110**, 116–128.
8 H. Shi, J. Frias, A. El-Din, H. Sayed, G. E. De-la-Torre, M.-C. Jong, S. A. Uddin, R. Rajaram, S. Chavanich, A. Najii, M. D. Fernández-Severini, Y. S. Ibrahim and L. Su, Small plastic fragments: A bridge between large plastic debris and micro- & nano-plastics, *TrAC, Trends Anal. Chem.*, 2023, **168**, 117308.
9 S. Monira, R. Roychand, M. A. Bhuiyan and B. K. Pramanik, Role of water shear force for microplastics fragmentation into nanoplastics, *Environ. Res.*, 2023, **237**, 116916.
10 P. García-Muñoz, P. H. Allé, C. Bertoloni, A. Torres, M. U. De La Orden, J. M. Urreaga, M.-A. Dziurla, F. Fresno, D. Robert and N. Keller, Photocatalytic degradation of polystyrene nanoplastics in water. A methodological study, *J. Environ. Chem. Eng.*, 2022, **10**, 108195.
11 L. P. Domínguez-Jaimes, E. I. Cedillo-González, E. Luévano-Hipólito, J. D. Acuña-Bedoya and J. M. Hernández-López, Degradation of primary nanoplastics by photocatalysis using different anodized TiO2 structures, *J. Hazard. Mater.*, 2021, **413**, 125452.
12 J. N. Hahladakis, C. A. Velis, R. Weber, E. Iacovidou and P. Purnell, An overview of chemical additives present in plastics: Migration, release, fate and environmental impact during their use, disposal and recycling, *J. Hazard. Mater.*, 2018, **344**, 179–199.
13 F. Yu, C. Yang, Z. Zhu, X. Bai and J. Ma, Adsorption behavior of organic pollutants and metals on micro/nanoplastics in the aquatic environment, *Sci. Total Environ.*, 2019, **694**, 133643.
14 Y. Yu, W. Y. Mo and T. Luukkonen, Adsorption behaviour and interaction of organic micropollutants with nano and microplastics – A review, *Sci. Total Environ.*, 2021, **797**, 149140.
15 V.-G. Le, M.-K. Nguyen, H.-L. Nguyen, C. Lin, M. Hadi, N. T. Q. Hung, H.-G. Hoang, K. N. Nguyen, H.-T. Tran, D. Hou, T. Zhang and N. S. Bolan, A comprehensive review of micro- and nano-plastics in the atmosphere: Occurrence, fate, toxicity, and strategies for risk reduction, *Sci. Total Environ.*, 2023, **904**, 166649.
16 V. Kumar, E. Singh, S. Singh, A. Pandey and P. C. Bhargava, Micro- and nano-plastics (MNPs) as emerging pollutant in ground water: Environmental impact, potential risks, limitations and way forward towards sustainable management, *Chem. Eng. J.*, 2023, **459**, 141568.
17 S. Lambert and M. Wagner, in *Freshwater Microplastics*, ed. M. Wagner and S. Lambert, Springer International Publishing, Cham, 2018, vol. 58, pp. 1–23.
18 A. S. Reddy and A. T. Nair, The fate of microplastics in wastewater treatment plants: An overview of source and remediation technologies, *Environ. Technol. Innovation*, 2022, **28**, 102815.
19 M. Sadia, A. Mahmood, M. Ibrahim, M. K. Irshad, A. H. A. Quddusi, A. Bokhari, M. Mubashir, L. F. Chuah and P. L. Show, Microplastics pollution from wastewater treatment plants: A critical review on challenges, detection, sustainable removal techniques and circular economy, *Environ. Technol. Innovation*, 2022, **28**, 102946.
20 K. Conley, A. Clum, J. Deepe, H. Lane and B. Beckingham, Wastewater treatment plants as a source of microplastics to an urban estuary: Removal efficiencies and loading per capita over one year, *Water Res.:X*, 2019, **3**, 100030.
21 S. H. Paiman, S. F. Md Noor, N. Ngadi, A. H. Nordin and N. Abdullah, Insight into photocatalysis technology as a promising approach to tackle microplastics pollution through degradation and upcycling, *Chem. Eng. J.*, 2023, **467**, 143534.
22 N. D. O. Dos Santos, R. Busquets and L. C. Campos, Insights into the removal of microplastics and microfibres by Advanced Oxidation Processes, *Sci. Total Environ.*, 2023, **861**, 160665.
23 R. Y. Krishnan, S. Manikandan, R. Subbaiya, N. Karmegam, W. Kim and M. Govarthanan, Recent approaches and advanced wastewater treatment technologies for mitigating emerging microplastics contamination – A critical review, *Sci. Total Environ.*, 2023, **858**, 159681.
24 N. A. Khan, A. H. Khan, E. A. López-Maldonado, S. S. Alam, J. R. López López, P. F. Méndez Herrera, B. A. Mohamed,

A. E. D. Mahmoud, A. Abutaleb and L. Singh, Microplastics: Occurrences, treatment methods, regulations and foreseen environmental impacts, *Environ. Res.*, 2022, **215**, 114224.

25 Z. Yang, Y. Li and G. Zhang, Degradation of microplastic in water by advanced oxidation processes, *Chemosphere*, 2024, **357**, 141939.

26 X. Shi, Z. Chen, X. Liu, W. Wei and B.-J. Ni, The photochemical behaviors of microplastics through the lens of reactive oxygen species: Photolysis mechanisms and enhancing photo-transformation of pollutants, *Sci. Total Environ.*, 2022, **846**, 157498.

27 S. Dong, X. Yan, Y. Yue, W. Li, W. Luo, Y. Wang, J. Sun, Y. Li, M. Liu and M. Fan, H2O2 concentration influenced the photoaging mechanism and kinetics of polystyrene microplastic under UV irradiation: Direct and indirect photolysis, *J. Cleaner Prod.*, 2022, **380**, 135046.

28 J. Ge, Z. Zhang, Z. Ouyang, M. Shang, P. Liu, H. Li and X. Guo, Photocatalytic degradation of (micro)plastics using TiO2-based and other catalysts: Properties, influencing factor, and mechanism, *Environ. Res.*, 2022, **209**, 112729.

29 Y. Kakuma, A. Y. Nosaka and Y. Nosaka, Difference in TiO_2 photocatalytic mechanism between rutile and anatase studied by the detection of active oxygen and surface species in water, *Phys. Chem. Chem. Phys.*, 2015, **17**, 18691–18698.

30 T. Luttrell, S. Halpegamage, J. Tao, A. Kramer, E. Sutter and M. Batzill, Why is anatase a better photocatalyst than rutile? - Model studies on epitaxial TiO2 films, *Sci. Rep.*, 2014, **4**, 4043.

31 V. Etacheri, C. Di Valentin, J. Schneider, D. Bahnemann and S. C. Pillai, Visible-light activation of TiO2 photocatalysts: Advances in theory and experiments, *J. Photochem. Photobiol., C*, 2015, **25**, 1–29.

32 R. Ghamarpoor, A. Fallah and M. Jamshidi, Investigating the use of titanium dioxide (TiO2) nanoparticles on the amount of protection against UV irradiation, *Sci. Rep.*, 2023, **13**, 9793.

33 J. Schneider, M. Matsuoka, M. Takeuchi, J. Zhang, Y. Horiuchi, M. Anpo and D. W. Bahnemann, Understanding TiO_2 Photocatalysis: Mechanisms and Materials, *Chem. Rev.*, 2014, **114**, 9919–9986.

34 Q. Guo, C. Zhou, Z. Ma and X. Yang, Fundamentals of TiO_2 Photocatalysis: Concepts, Mechanisms, and Challenges, *Adv. Mater.*, 2019, **31**, 1901997.

35 D. Chen, Y. Cheng, N. Zhou, P. Chen, Y. Wang, K. Li, S. Huo, P. Cheng, P. Peng, R. Zhang, L. Wang, H. Liu, Y. Liu and R. Ruan, Photocatalytic degradation of organic pollutants using TiO2-based photocatalysts: A review, *J. Cleaner Prod.*, 2020, **268**, 121725.

36 P. Jiang, T. Zhou, J. Bai, Y. Zhang, J. Li, C. Zhou and B. Zhou, Nitrogen-containing wastewater fuel cells for total nitrogen removal and energy recovery based on Cl·/ClO· oxidation of ammonia nitrogen, *Water Res.*, 2023, **235**, 119914.

37 W. R. Siah, H. O. Lintang, M. Shamsuddin and L. Yuliati, High photocatalytic activity of mixed anatase-rutile phases on commercial TiO_2 nanoparticles, *IOP Conf. Ser.:Mater. Sci. Eng.*, 2016, **107**, 012005.

38 K. Almashhori, T. T. Ali, A. Saeed, R. Alwafi, M. Aly and F. E. Al-Hazmi, Antibacterial and photocatalytic activities of controllable (anatase/rutile) mixed phase TiO_2 nanophotocatalysts synthesized *via* a microwave-assisted sol–gel method, *New J. Chem.*, 2020, **44**, 562–570.

39 Y. Zhang, J. Chen and X. Li, Preparation and Photocatalytic Performance of Anatase/Rutile Mixed-Phase TiO2 Nanotubes, *Catal. Lett.*, 2010, **139**, 129–133.

40 N. R. Reddy, P. M. Reddy, N. Jyothi, A. S. Kumar, J. H. Jung and S. W. Joo, Versatile TiO2 bandgap modification with metal, non-metal, noble metal, carbon material, and semiconductor for the photoelectrochemical water splitting and photocatalytic dye degradation performance, *J. Alloys Compd.*, 2023, **935**, 167713.

41 T. Zhou, J. Wang, S. Chen, J. Bai, J. Li, Y. Zhang, L. Li, L. Xia, M. Rahim, Q. Xu and B. Zhou, Bird-nest structured ZnO/TiO2 as a direct Z-scheme photoanode with enhanced light harvesting and carriers kinetics for highly efficient and stable photoelectrochemical water splitting, *Appl. Catal., B*, 2020, **267**, 118599.

42 T. Zhou, S. Chen, L. Li, J. Wang, Y. Zhang, J. Li, J. Bai, L. Xia, Q. Xu, M. Rahim and B. Zhou, Carbon quantum dots modified anatase/rutile TiO2 photoanode with dramatically enhanced photoelectrochemical performance, *Appl. Catal., B*, 2020, **269**, 118776.

43 T. Zhou, L. Li, J. Li, J. Wang, J. Bai, L. Xia, Q. Xu and B. Zhou, Electrochemically reduced TiO2 photoanode coupled with oxygen vacancy-rich carbon quantum dots for synergistically improving photoelectrochemical performance, *Chem. Eng. J.*, 2021, **425**, 131770.

44 S. Gowrisankaran, G. K. Thirunavukkarasu, H. Makarov, T. Roch, G. Plesch, M. Motola, G. Mailhot, M. Brigante and O. Monfort, New insights into the mechanism of coupled photocatalysis and Fenton-based processes using Fe surface-modified TiO2 nanotube layers: The case study of caffeine degradation, *Catal. Today*, 2023, **413–415**, 114027.

45 J. P. Ribeiro and M. I. Nunes, Recent trends and developments in Fenton processes for industrial wastewater treatment – A critical review, *Environ. Res.*, 2021, **197**, 110957.

46 M. I. Maldonado, P. C. Passarinho, I. Oller, W. Gernjak, P. Fernández, J. Blanco and S. Malato, Photocatalytic degradation of EU priority substances: A comparison between TiO2 and Fenton plus photo-Fenton in a solar pilot plant, *J. Photochem. Photobiol., A*, 2007, **185**, 354–363.

47 D. Ortiz, M. Munoz, J. Nieto-Sandoval, C. Romera-Castillo, Z. M. De Pedro and J. A. Casas, Insights into the degradation of microplastics by Fenton oxidation: From surface modification to mineralization, *Chemosphere*, 2022, **309**, 136809.

48 B. Liu, Q. Jiang, Z. Qiu, L. Liu, R. Wei, X. Zhang and H. Xu, Process analysis of microplastic degradation using activated PMS and Fenton reagents, *Chemosphere*, 2022, **298**, 134220.

49 K. Kik, B. Bukowska and P. Sicińska, Polystyrene nanoparticles: Sources, occurrence in the environment, distribution in tissues, accumulation and toxicity to various organisms, *Environ. Pollut.*, 2020, **262**, 114297.

50 D. Barceló, Y. Picó and A. H. Alfarhan, Microplastics: Detection in human samples, cell line studies, and health impacts, *Environ. Toxicol. Pharmacol.*, 2023, **101**, 104204.
51 C. Zhang, J. W. Chung and R. D. Priestley, Dialysis Nanoprecipitation of Polystyrene Nanoparticles, *Macromol. Rapid Commun.*, 2012, **33**, 1798–1803.
52 B. Komárková, M. Motlochová, V. Slovák, P. Ecorchard, P. Bezdička, D. Bavol and J. Šubrt, Effect of amines on (peroxo) titanates: characterization and thermal decomposition, *J. Therm. Anal. Calorim.*, 2022, **147**, 5009–5022.
53 G. K. Thirunavukkarasu, O. Monfort, M. Motola, M. Motlochová, M. Gregor, T. Roch, M. Čaplovicová, A. Y. Lavrikova, K. Hensel, V. Brezová, M. Jerigová, J. Šubrt and G. Plesch, Ce ion surface-modified TiO_2 aerogel powders: a comprehensive study of their excellent photocatalytic efficiency in organic pollutant removal, *New J. Chem.*, 2021, **45**, 4174–4184.
54 H.-M. Feng, J.-C. Zheng, N.-Y. Lei, L. Yu, K. H.-K. Kong, H.-Q. Yu, T.-C. Lau and M. H. W. Lam, Photoassisted Fenton Degradation of Polystyrene, *Environ. Sci. Technol.*, 2011, **45**, 744–750.
55 W.-K. Wang, J.-J. Chen, X. Zhang, Y.-X. Huang, W.-W. Li and H.-Q. Yu, Self-induced synthesis of phase-junction TiO2 with a tailored rutile to anatase ratio below phase transition temperature, *Sci. Rep.*, 2016, **6**, 20491.
56 M. Buchalska, M. Kobielusz, A. Matuszek, M. Pacia, S. Wojtyła and W. Macyk, On Oxygen Activation at Rutile- and Anatase-TiO_2, *ACS Catal.*, 2015, **5**, 7424–7431.
57 I. Nabi, A.-U.-R. Bacha, K. Li, H. Cheng, T. Wang, Y. Liu, S. Ajmal, Y. Yang, Y. Feng and L. Zhang, Complete Photocatalytic Mineralization of Microplastic on TiO2 Nanoparticle Film, *iScience*, 2020, **23**, 101326.
58 G. K. Thirunavukkarasu, S. Gowrisankaran, M. Caplovicova, L. Satrapinskyy, M. Gregor, A. Lavrikova, J. Gregus, R. Halko, G. Plesch, M. Motola and O. Monfort, Contribution of photocatalytic and Fenton-based processes in nanotwin structured anodic TiO_2 nanotube layers modified by Ce and V, *Dalton Trans.*, 2022, **51**, 10763–10772.
59 I. Konstantinou, Photocatalytic transformation of pesticides in aqueous titanium dioxide suspensions using artificial and solar light: intermediates and degradation pathways, *Appl. Catal., B*, 2003, **42**, 319–335.
60 E. Yousif and R. Haddad, Photodegradation and photostabilization of polymers, especially polystyrene: review, *Springerplus*, 2013, **2**, 398.
61 T. J. Kemp and R. A. McIntyre, Influence of transition metal-doped titanium(IV) dioxide on the photodegradation of polystyrene, *Polym. Degrad. Stab.*, 2006, **91**, 3010–3019.
62 S. Goldstein, D. Aschengrau, Y. Diamant and J. Rabani, Photolysis of Aqueous H_2O_2 : Quantum Yield and Applications for Polychromatic UV Actinometry in Photoreactors, *Environ. Sci. Technol.*, 2007, **41**, 7486–7490.
63 A. L. Andrady, J. E. Pegram and Y. Tropsha, Changes in carbonyl index and average molecular weight on embrittlement of enhanced-photodegradable polyethylenes, *J. Environ. Polym. Degrad.*, 1993, **1**, 171–179.
64 M. Ghanadi and L. P. Padhye, Revealing the long-term impact of photodegradation and fragmentation on HDPE in the marine environment: Origins of microplastics and dissolved organics, *J. Hazard. Mater.*, 2024, **465**, 133509.
65 C. Srivastava, B. Alcock, A. Strandlie and S. A. Grammatikos, Comparison of the effect of thermal and hygrothermal sub-Tg aging on the durability and appearance of multilayered filament wound composite structure, *Polym. Test.*, 2024, **131**, 108326.
66 M. Palkovská, V. Slovák, J. Šubrt, J. Boháček and J. Havlín, Thermal decomposition of a peroxopolytitanic acid cryogel: TA/MS study, *Thermochim. Acta*, 2017, **647**, 1–7.
67 B. Komárková, P. Ecorchard, M. Motlochová, V. Slovák, X. Vislocká, D. Smržová, M. Kormunda, P. Bezdička, K. Lušpai, M. Šimunková, D. Dvoranová, M. Šrámová Slušná, L. Belháčová and J. Šubrt, Effect of amines on the peroxo-titanates and photoactivity of annealed TiO2, *Arabian J. Chem.*, 2022, **15**, 103808.
68 E. Dümichen, P. Eisentraut, C. G. Bannick, A.-K. Barthel, R. Senz and U. Braun, Fast identification of microplastics in complex environmental samples by a thermal degradation method, *Chemosphere*, 2017, **174**, 572–584.
69 J. Wang, J. Lee, E. E. Kwon and S. Jeong, Quantitative analysis of polystyrene microplastic and styrene monomer released from plastic food containers, *Heliyon*, 2023, **9**, e15787.
70 J. Rieger, The glass transition temperature of polystyrene: Results of a round robin test, *J. Therm. Anal.*, 1996, **46**, 965–972.
71 H. Xu and L. B. Casabianca, Probing driving forces for binding between nanoparticles and amino acids by saturation-transfer difference NMR, *Sci. Rep.*, 2020, **10**, 12351.
72 A. Homola and R. O. James, Preparation and characterization of amphoteric polystyrene latices, *J. Colloid Interface Sci.*, 1977, **59**, 123–134.
73 F. M. Onaga Medina, M. B. Aguiar, M. E. Parolo and M. J. Avena, Insights of competitive adsorption on activated carbon of binary caffeine and diclofenac solutions, *J. Environ. Manage.*, 2021, **278**, 111523.
74 B. Babić, J. Gulicovski, Z. Dohčević-Mitrović, D. Bučevac, M. Prekajski, J. Zagorac and B. Matović, Synthesis and characterization of Fe3+ doped titanium dioxide nanopowders, *Ceram. Int.*, 2012, **38**, 635–640.
75 M. Francoeur, A. Ferino-Pérez, C. Yacou, C. Jean-Marius, E. Emmanuel, Y. Chérémond, U. Jauregui-Haza and S. Gaspard, Activated carbon synthetized from Sargassum (sp) for adsorption of caffeine: Understanding the adsorption mechanism using molecular modeling, *J. Environ. Chem. Eng.*, 2021, **9**, 104795.
76 M. Ptaszkowska-Koniarz, J. Goscianska and R. Pietrzak, Synthesis of carbon xerogels modified with amine groups and copper for efficient adsorption of caffeine, *Chem. Eng. J.*, 2018, **345**, 13–21.
77 F. Azeez, E. Al-Hetlani, M. Arafa, Y. Abdelmonem, A. A. Nazeer, M. O. Amin and M. Madkour, The effect of surface charge on photocatalytic degradation of methylene blue dye using chargeable titania nanoparticles, *Sci. Rep.*, 2018, **8**, 7104.

78 A. Ceccarini, A. Corti, F. Erba, F. Modugno, J. La Nasa, S. Bianchi and V. Castelvetro, The Hidden Microplastics: New Insights and Figures from the Thorough Separation and Characterization of Microplastics and of Their Degradation Byproducts in Coastal Sediments, *Environ. Sci. Technol.*, 2018, **52**, 5634–5643.

79 D. Dvoranová, Z. Barbieriková and V. Brezová, Radical Intermediates in Photoinduced Reactions on TiO2 (An EPR Spin Trapping Study), *Molecules*, 2014, **19**, 17279–17304.

80 Z. Barbieriková, D. Dvoranová and V. Brezová, in *Materials Science in Photocatalysis*, Elsevier, 2021, pp. 125–138.

81 J. R. Harbour, J. Tromp and M. L. Hair, Photogeneration of hydrogen peroxide in aqueous TiO_2 dispersions, *Can. J. Chem.*, 1985, **63**, 204–208.

82 I. Papailias, N. Todorova, T. Giannakopoulou, D. Dvoranová, V. Brezová, D. Dimotikali and C. Trapalis, Selective removal of organic and inorganic air pollutants by adjusting the g-C3N4/TiO2 ratio, *Catal. Today*, 2021, **361**, 37–42.

83 C. Wang, R. Sun, R. Huang and H. Wang, Superior fenton-like degradation of tetracycline by iron loaded graphitic carbon derived from microplastics: Synthesis, catalytic performance, and mechanism, *Sep. Purif. Technol.*, 2021, **270**, 118773.

84 I. Gutiérrez, S. G. Bertolotti, M. A. Biasutti, A. T. Soltermann and N. A. García, Quinones and hydroxyquinones as generators and quenchers of singlet molecular oxygen, *Can. J. Chem.*, 1997, **75**, 423–428.

85 X. Zheng, J. Yuan, J. Shen, J. Liang, J. Che, B. Tang, G. He and H. Chen, A carnation-like rGO/Bi2O2CO3/BiOCl composite: efficient photocatalyst for the degradation of ciprofloxacin, *J. Mater. Sci.: Mater. Electron.*, 2019, **30**, 5986–5994.

